Published in final edited form as:
Am J Physiol Heart Circ Physiol. 2003 September ; 285(3): H1303–H1316. doi:10.1152/ajpheart.00933.2001.

An integrative model of coupled water and solute exchange in the heart

Michael R. Kellen and **James B. Bassingthwaighte**
Department of Bioengineering, University of Washington, Seattle, Washington 98195

Abstract

Physiologists have devised many models for interpreting water and solute exchange data in whole organs, but the models have typically neglected key aspects of the underlying physiology to present the simplest possible model for a given experimental situation. We have developed a physiologically realistic model of microcirculatory water and solute exchange and applied it to diverse observations of water and solute exchange in the heart. Model simulations are consistent with the results of osmotic weight transient, tracer indicator dilution, and steady-state lymph sampling experiments. The key model features that permit this unification are the use of an axially distributed blood-tissue exchange region, inclusion of a lymphatic drain in the interstitium, and the independent computation of transcapillary solute and solvent fluxes through three different pathways.

Keywords

microcirculation; capillary permeability; osmotic transient; lymph; multiple-indicator dilution

Physiologists are interested in the exchange of material between capillaries and their surrounding tissues because this process is fundamental to the viability of multicellular life. The kinetics of coupled solute-solvent exchange across capillary walls can be described phenomenologically by three parameters: the hydraulic conductivity (L_p), the permeability (P), and the reflection coefficient (σ) (37). The values of these parameters can be determined by several experimental methods, including measurement of the outflow concentration time courses of solutes after a bolus injection of tracers (the multiple-tracer indicator dilution technique), gravimetric or isogravimetric measurements of the response to perturbations of osmotic or hydrostatic pressures (the osmotic transient method), and simultaneous measurements of solute concentrations in lymph and plasma (lymph sampling techniques). Reasonable fits to data from these sources have been obtained with relatively simple analytical methods, like the Crone-Renkin (18,52) estimate of capillary permeability, the Vargas and Johnson (65) estimate of reflection coefficient, and the “pore-stripping” analysis of Renkin et al. (52a). These analysis methods have enjoyed widespread use in determining transport parameter values from indicator dilution, osmotic transient, and lymph data, respectively.

Although mathematically independent, all three phenomenological transport parameters must ultimately arise from the physical and chemical properties of the exchanging solution and the anatomic structures that create the pathways for its exchange across capillary walls. Consequently, hydrodynamic models of solute and fluid movements through the endothelial

Address for reprint requests and other correspondence: J. Bassingthwaighte, Univ. of Washington, Bioengineering, Box 357962, Seattle, WA 98195-7962 (jbb@bioeng.washington.edu).

cell junction, represented as idealized pores in the capillary wall, have been developed to relate the transport parameters to mechanistic quantities such as solute size and diffusion coefficient and pore radius and relative area (12,19,44,48,49). Even though there is no strict correspondence between the idealized pores and actual capillary morphology, pore models have proven useful as both a unified description of diverse sets of exchange data and a constraint on the possible values of the transport parameters. Models of capillary walls typically contain three pore systems: a small-pore system corresponding to the endothelial junction, a large-pore system through vesicles or infrequent breaks in the capillary wall structure, and a pathway for water only interpreted as transport across the endothelial cell membranes. More recently, three-dimensional models of the cleft and surface glycocalyx, derived from the actual morphology of the capillary wall, have provided a more detailed description of paracellular fluid and solute flows and ascribed at least some of the resistance to exchange to endothelial glycocalyx rather than the cleft walls (25,34).

However, the results of simple analysis methods for different experiments, looked at together and interpreted by pore theory, lead to apparent contradictions. Using Crone's method for estimating the product of capillary permeability and surface area (*PS*), Alvarez and Yudilevich (3) observed that the ratios of solute permeability to free diffusion coefficient (*P/D*) were very nearly the same for urea, glycerol, glucose, sucrose, and inulin. This fact was confirmed by other researchers using the same technique (10,45), and refinements of the methods for tracer analysis have not changed the observation (9). This result implies that permeation of these solutes is dependent only on the solute diffusion coefficient and not on any steric hindrance due to glycocalyx or cell walls; the cleft widths between adjacent endothelial cells must be at least 10–20 nm for this to be true. Size-independent *P/D* for small hydrophilic solutes is consistent with the 20-nm widths of the endothelial junction observed with serial-section electron microscopy (15).

On the other hand, osmotic transient experiments in whole organs (27,64,65,69) and in single capillaries (21) showed that even the smallest hydrophilic solutes induced transient transcapillary water exchange, demonstrating that their passage across the capillary wall was hindered relative to water. Small-solute reflection coefficients were nonzero and weakly size dependent, implying relative steric hindrance of the same molecules that showed size-independent permeability estimates. Pappenheimer et al. (49) interpreted similar data from an isogravimetric hindlimb preparation as requiring a cleft with an equivalent pore width of 6 nm to make the junction a molecular size-dependent filter. The postulation of an additional pathway for solute-free water exchange, occurring in parallel to the pathway for coupled water and solute exchange through the endothelial cleft, has partially resolved the problem by explaining nonzero reflection coefficients as an averaging between selective and nonselective pathways.

Even detailed models of the endothelial junction and surface glycocalyx do not adequately explain osmotically driven water fluxes arising from small solutes because the 7-nm spacing of glycocalyx fibers is too wide to generate a significant osmotic pressure; the addition of a separate transcellular pathway only for water will be necessary before these types of models can be considered complete. The evidence supporting a distinct pathway for water flux is clear; Effros (22) demonstrated that the fluid extracted from lung tissues during an increase in perfusate osmolarity was essentially solute free, implying the existence of an additional, presumably transcellular, pathway across the capillary. The recent identification of the ubiquitous expression of aquaporin water channels in the endothelial cells of most organs (66) and the demonstration that the movement of osmotically driven water exchange can be inhibited by known inhibitors of aquaporins (16,23) have precisely identified the molecular basis for solute-free water movements.

In the present study, we developed a model of the transcapillary exchange process that successfully reproduces data obtained from osmotic transient, multiple-tracer dilution, and lymph sampling methods in whole hearts. The unification of the three major types of data on solute and water exchange in whole organs is the major contribution of this work.

Model

Microcirculatory exchange (Fig. 1) consists of the coupled transcapillary exchange of fluid (J_{Vc}) and solutes (J_s), lymphatic drainage of interstitial fluid (F_L), and water exchange across the parenchymal cell membrane (J_{Vpc}). These fluxes determine changes in the fluid volumes of interstitium ($V_{f,isf}$) and parenchymal cells ($V_{f,pc}$), perfusate velocities (u) in a constant-volume capillary, and solute quantities of N_s different solutes in all three regions ($n_{c,j}$, $n_{isf,j}$, and $n_{pc,j}$)

$$\frac{\partial u}{\partial x}=\frac{-S_c J_{Vc}}{V_c} \text{ for } J_{vc}=J_{v,endo}+J_{v,sp}+J_{v,lp} \tag{1}$$

$$\frac{\partial V_{f,isf}}{\partial t}=S_c J_{Vc}+S_{pc} J_{Vpc}-F_L \tag{2}$$

$$\frac{\partial V_{f,pc}}{\partial t}=-S_{pc} J_{Vpc} \tag{3}$$

$$\frac{\partial n_{c,j}}{\partial t}=-\frac{\partial}{\partial x}(u\cdot n_{c,j})-S_c J_{s,j} \text{ for } j=1-N_s \tag{4}$$

$$\frac{\partial n_{isf,j}}{\partial t}=S_c J_{s,j}-F_L C'_{isf,j} \text{ for } j=1-N_s \tag{5}$$

$$\frac{\partial n_{pc,j}}{\partial t}=0 \text{ for } j=1-N_s \tag{6}$$

where the physiological variables are assumed to be functions of time (t) and one spatial dimension (x). S_c and S_{pc} are surface areas of capillaries and parenchymal cells, respectively, and C'_{isf} is an effective solute concentration in the interstitium. Solute exchange across parenchymal cell membrane is set to zero because transplasmalemmal fluxes of most hydrophilic solutes do not occur; even glucose transport is very small (40). The following sections expand on this foundation by providing more specific definitions of the terms used and by relating perturbations in organ-level flows, pressures, or perfusate composition to changes in fluid and solute fluxes at the microvascular level.

Pressure-flow relationship in vascular networks

Because capillary hydrostatic pressure cannot be measured directly in intact organs, a relationship must be defined between this quantity and observable variables such as flow,

arterial pressure, and venous pressure. The organ's vasculature is modeled with lumped hydraulic resistances (Ω) to represent different portions of the vascular network, as shown in Fig. 2A. The relationship between arterial pressure (p_a), venous pressure (p_v), and flow (F) at any given time is

$$p_a - p_v = F(\Omega_a + \Omega_c + \Omega_v) \tag{7}$$

where Ω_a, Ω_c, and Ω_v are arterial, capillary, and venous hydraulic resistances. Under many experimental situations p_a, p_v, and F are measurable, allowing calculation of the total vascular resistance from Eq. 7 (Fig. 2B). The relative distribution of vascular resistances for the heart (17) and the known geometry of the coronary capillary bed can be used to estimate Ω_c and Ω_v. The capillary inlet (p_{ci}) and outlet pressures (p_{co}) are then

$$p_{ci} = F(\Omega_c + \Omega_v) + p_v \tag{8}$$

$$p_{co} = F\Omega_v + p_v \tag{9}$$

The fluid flow in veins is reduced by net filtration (J_v) from capillary to interstitium. Because the maximal values of J_v, obtained during the initial phase of an osmotic transient experiment, are <0.1 ml·min^{-1}·g^{-1} compared with F of at least 2 ml·min^{-1}·g^{-1}, Eqs. 8 and 9 are good approximations. These pressures and flows should be understood as mean values averaged over the cardiac cycle; cyclic flows caused by cardiac contraction have a negligible effect on the rate of solute equilibration between perfusate and interstitial fluid (8) and occur over a faster time scale than exchange processes. Pressures and flows also vary as hydraulic resistance is modulated by changes in transmural pressure and neuronal, humoral, and myogenic regulation, but detailed descriptions of these phenomena are beyond the current scope of the model.

Cardiac tissue organization

The organ volume is taken to consist of large vessels and a symmetrical array of blood-tissue exchange (BTEX) units composed of a capillary and surrounding tissue. The relationships between the dimensions of the BTEX unit (see Fig. 3) and the initial anatomic volumes (v) and surface areas for exchange (*S*) of the capillary, interstitial, and parenchymal cell subregions are

$$v_{btex} = \frac{\sqrt{3}}{2} d_{ic}^2 l_c \tag{10}$$

$$v_c = \pi r_c^2 l_c \tag{11}$$

$$v_{isf} = \pi[(r_c + d_{im})^2 - r_c^2] l_c + 2[d_{ic} - 2(r_c + d_{im})] d_{im} l_c \tag{12}$$

$$v_{pc}=v_{btex}-v_{isf}-v_c \tag{13}$$

$$S_c=2\pi r_c l_c \tag{14}$$

$$S_{pc}=2l_c\pi(r_c+d_{im})-4l_c d_{im}+4l_c[d_{ic}-2(r_c+d_{im})] \tag{15}$$

where d_{ic} and d_{im} are distance between capillaries and distance between myocytes or between capillaries and myocytes, respectively, and l_c and r_c are capillary length and radius, respectively. The interstitium and myocardial cells are modeled as a composite of fluid and solid phases uniformly distributed throughout the region. The solids present in cardiac tissue are predominantly collagen (subscript col) and other matrix proteins (subscript im) in the interstitium and myofilaments and other large protein structures in the cells. The fluid volume and solid volumes in each region (V_f and V_s) are

$$V_{f,c}=v_c \tag{16}$$

$$V_{s,isf}=v_{isf}\frac{Q_{im}+Q_{col}}{\rho_s} \tag{17}$$

$$V_{f,isf}=v_{isf}-V_{s,isf} \tag{18}$$

$$V_{s,pc}=v_{pc}\frac{Q_{pc}}{\rho_s} \tag{19}$$

$$V_{f,pc}=v_{pc}-V_{s,pc} \tag{20}$$

where Q_{col} is the quantity of interstitial collagen per unit interstitial volume, Q_{im} is the quantity of other interstitial matrix proteins per unit interstitial volume, Q_{pc} is the cellular quantity of solid protein components per unit cellular volume, and ρ_s is the density of the solid components.

Changes in volumes at the level of BTEX units are related to more readily observable whole organ quantities (see Table 1). On a whole organ basis, if the volume fraction of the large vessels is $\dot{V}_{lv}$, the fractional volumes ($\dot{V}_i$, ml of *i*/ml of org) of the capillary (cap), interstitial (isf), and myocyte (pc) regions are

$$\dot{V}_i=(1-\dot{V}_{lv})\frac{V_i}{v_{btex}} \tag{21}$$

for i = cap, isf, or pc fluid or solid volumes. The density of the organ (ρ_{org}) can then be computed from

$$\rho_{org}=\rho_f\dot{V}_{lv}+\sum_i(\rho_f\dot{V}_{f,i}+\rho_s\dot{V}_{s,i}) \tag{22}$$

Specific volumes and surface areas ($\hat{V}$, ml/g of tissue and $\hat{S}$, cm^2/g of tissue) are

$$\widehat{V}_i=\frac{\dot{V}_i}{\rho_{org}} \tag{23}$$

$$\widehat{S}_i=\frac{S_i}{V_{btex}}\frac{(1-\dot{V}_{lv})}{\rho_{org}} \tag{24}$$

for i = c or pc, and the number of capillaries per unit organ mass ($\hat{N}_c$) is

$$\widehat{N}_c=\frac{\widehat{V}_c}{v_c} \tag{25}$$

The total number of capillaries in the organ (N_c) remains constant as the product of $\hat{N}_{cap}$ and the initial organ weight, W^o; capillary recruitment is not considered. The weight of the organ as a function of time [$W(t)$] can be found by adding the weights of each region. The weight of the solid components and vascular regions is constant, so any observed weight change of the organ is caused by fluid loss or gain in the interstitium or parenchymal cells

$$W(t)=N_c[(V_{cap}+V_{f,isf}+V_{f,pc})\rho_f+(V_{s,isf}+V_{s,pc})\rho_s]+\widehat{V}^o_{vas}\rho_f W^o \tag{26}$$

The tissue model can also be used to estimate the hydraulic resistance of the capillary bed, assuming Poiseuille flow through the bed of parallel cylindrical capillaries

$$\Omega_c=\left(\frac{8\eta l_c}{\pi r_c^4}\right)\frac{1}{N_c} \tag{27}$$

Fluid exchange

Transcapillary fluid exchange occurs through multiple parallel pathways that are treated purely phenomenologically in this section. The volume flux through the kth pathway from capillary to interstitium (J_{vk}) as a function of axial position in the capillary is given by

$$J_{Vk}=L_{pk}\left\{(p_c - p_{isf}) - \sum_j [\sigma_{j,k}(\Pi_{c,j} - \Pi_{isf,j})]+\Pi_M\right\} \quad (28)$$

where L_{pk} is the hydraulic conductivity through the kth pathway, $\sigma_{j,k}$ is the reflection coefficient of the jth solute in the kth pathway, $\Pi_{c,j}$ and $\Pi_{isf,j}$ are the osmotic pressures of the jth solute in capillary and interstitium, and Π_M is the osmotic pressure exerted by interstitial matrix proteins. The total transcapillary flux (J_{vc}) is then the sum of the individual pathways

$$J_{Vc}=\sum_k J_{Vk}=J_{V,endo}+J_{V,sp}+J_{V,lp} \quad (29)$$

The osmotic pressures of the mobile solutes in each region are described empirically by the virial expansion

$$\Pi_j=RT(\varphi_{1,j}C'_j+\varphi_{2,j}C'^{2}_j+\varphi_{3,j}C'^{3}_j) \quad (30)$$

where ϕ_n is the nth virial coefficient. This expression contains no solute-solute interaction terms, although these interactions are implied by nonzero second and third virial coefficients. The virial coefficients for one solute should therefore strictly be considered to be a function of the concentrations of all other solutes. In practice, we consider only one solute (albumin) with nonzero terms beyond the first virial coefficient, so this difficulty is avoided.

The effective concentration (C′) is

$$C'_j=\frac{n_j}{\gamma_j V_f} \quad (31)$$

which accounts for the exclusion of the solute from a certain fraction (γ) of the interstitial space by the interstitial matrix fibers. This fraction is dependent on the solute radius (r_j) and fiber quantity (Q_{im} or Q_{col}), radius (r_f), and density (ρ) (20)

$$\gamma_j=\exp\left[-\frac{Q_{im}}{\rho_{im}}\left(\frac{2r_j}{r_{f,im}}+\frac{r_j^2}{r_{f,im}^2}\right)\right]\exp\left[-\frac{Q_{col}}{\rho_{col}}\left(\frac{2r_j}{r_{f,col}}+\frac{r_j^2}{r_{f,col}^2}\right)\right] \quad (32)$$

Distribution effects are neglected in the parenchymal cells, where only total cell osmolarity, not concentrations of individual species, are modeled.

In addition to the osmotic pressure of the solutes present in plasma and interstitial fluid, interstitial matrix components, especially hyaluronate, exhibit a significant osmotic pressure, as evidenced by the reduction in tissue water after enzymatic digestion of this molecule (60). The osmotic pressure of the immobile interstitial matrix components (Π_M) is given by the empirical relationship

$$\Pi_M=\psi_1 Q_{im}+\psi_2 Q_{im}^2+\psi_3 Q_{im}^3 \tag{33}$$

where ψ_n is the nth matrix osmotic pressure coefficient. Similarly, the water flux across the parenchymal cell membrane from cells to interstitium is given by

$$J_{V,pc}=L_{p,pc}\left[(p_{pc}-p_{isf})-\left(\Pi_{pc}-\Pi_M-\sum_j \Pi_{isf,j}\right)\right] \tag{34}$$

High interstitial pressures and low lymphatic outlet pressures promote drainage of the interstitium through the lymphatics, and the presence of valves in the lymphatic vessels prevents back flow (41,55). These facts lead to an empirical relationship between interstitial pressure and lymph flow (F_L)

$$F_L=K_L(p_{isf}-p_L) \text{ for } p_{isf}>p_L \tag{35}$$

$$F_L=0 \text{ for } p_{isf}\le p_L \tag{36}$$

where K_L is lymphatic conductance. Capillary hydrostatic pressure is modeled as a linear gradient with end points set by the whole organ pressure-flow relationship. When water enters or leaves the capillary, changes in the perfusate flow velocity along the capillary length alter this relationship. Net transcapillary water exchange is negligible compared with axial convection, however, so the linear gradient remains a reasonable approximation. Interstitial and parenchymal cell hydrostatic pressures are in general functions of the change in volume of these regions and are modeled with an empirical formula

$$p_c(x)=p_{co}+(p_{ci}-p_{co})\left(\frac{l_c-x}{l_c}\right) \tag{37}$$

$$p_{isf}=p_{isf}^o+\Delta V_{isf}(E_1+E_2|\Delta V_{isf}|+E_3\Delta V_{isf}^2) \tag{38}$$

$$p_{pc}=p_{pc}^o+\Delta V_{pc}(E_1+E_2|\Delta V_{pc}|+E_3\Delta V_{pc}^2) \tag{39}$$

where E_n is the nth elastance coefficient. Here ΔV is defined as a fractional change in volume compared with the initial value

$$\Delta V_i=\frac{V_i-V_i^o}{V_i^o} \tag{40}$$

As a practical matter, terms beyond E_1 are small enough that one can assume a constant compliance, at least over a relatively small range of volume changes. With marked edema, the interstitium may reach a yield point at which compliance rapidly increases and the linear model is no longer appropriate.

Capillary flows are assumed to be homogeneous, so the perfusate velocity at the capillary inlet is given by the boundary condition

$$u(t, x=0)=\frac{\mathrm{F}(t)}{N_{\mathrm{c}}\pi r_{\mathrm{c}}^2} \tag{41}$$

Solute exchange

Solute fluxes are calculated from the nonlinear solute flux equation developed by Patlak et al. (50). This equation correctly accounts for the coupling between convective and diffusive flux that occurs when convection alters the quasi-steady-state concentration profile within the membrane. The total solute flux of solute j from capillary to interstitium, $J_{\mathrm{s},j}$, is given by the sum of diffusive and convective transport for each path

$$J_{\mathrm{s},j}=\sum_k \left[J_{\mathrm{v}k}(1-\sigma_{j,k})\mathrm{C}_{\mathrm{c},j}+P_{j,k}(\mathrm{C}_{\mathrm{c},j}-\mathrm{C}_{\mathrm{isf},j})\left(\frac{\mathrm{Pe}_{j,k}}{e^{\mathrm{Pe}_{j,k}}-1}\right)\right] \tag{42}$$

$\mathrm{Pe}_{j,k}$ is the Péclet number for the jth solute traveling through the kth pathway, defined by

$$\mathrm{Pe}_{j,k}\frac{J_{\mathrm{v}k}(1-\sigma_{j,k})}{P_{j,k}} \tag{43}$$

The boundary conditions at the capillary inlet for solute are

$$\frac{\mathrm{d}}{\mathrm{d}t}n_{\mathrm{c},j}(t, x=0)=\mathrm{C}_{ci,j}(t)\mathrm{F}(t) \tag{44}$$

Pathways for transcapillary exchange

Although transcapillary exchange can be calculated if a complete set of phenomenological coefficients is given, the number of parameters that must be specified soon becomes unwieldy for physiologically realistic conditions. A mechanistic model of each pathway for exchange provides a constraint that limits the values that these parameters can take. Two pathways for solute and water exchange are modeled as cylindrical pores that permit the passage of spherical solutes following the equations derived by Bean (12) to relate L_{p}, P, and σ to pore and solute geometry

$$L_{\mathrm{p}}=\left(\frac{A_{\mathrm{p}}}{S_{\mathrm{c}}\Delta r}\right)\frac{r_{\mathrm{p}}^2}{8\eta} \tag{45}$$

$$P=\left(\frac{A_p}{S_c\Delta r}\right)(1-\alpha)F(\alpha)D \tag{46}$$

$$\sigma=1-\{1-[1-(1-\alpha)^2]^2\}G(\alpha) +\tfrac{16}{9}\alpha^2(1-\alpha)^2F(\alpha) \tag{47}$$

with $\alpha = r_s/r_p$. Values of the hydrodynamic functions $F(\alpha)$ and $G(\alpha)$ are given in Table 1 and more completely derived in Curry's review (20). An additional pathway exclusive to water ($P = 0$, $\sigma = 1$ for all solutes), representing transport across the endothelial cell plasmalemma, is defined by a single value of $L_{p,endo}$ and the flux is $J_{v,endo}$ (Fig. 1).

Numerical methods

The numerical solution to the system of the partial differential equations was obtained by discretizing the blood-tissue exchange unit in space and separating axial convection from radial exchange (Fig. 4). The model time step was defined as the time for convection to move the capillary fluid exactly one axial segment downstream in the absence of transcapillary fluid exchange (6,9)

$$\Delta t=\frac{N_c V_c}{F N_{seg}} \tag{48}$$

where N_c is the number of capillaries in the whole organ and N_{seq} is the number of axial segments in a BTEX unit. Radial transfers among the cellular, interstitial, and capillary regions are computed for each axial segment with a numerical ordinary differential equation (ODE) solver, either DOPRI5, a fifth-order Runge-Kutta method with adaptive step size, or RADAU, a stiff ODE solver (29,30). The model was developed with XSIM, a modeling environment developed by the National Simulation Resource for Circulatory Mass Transport (http://nsr.bioeng.washington.edu).

The accuracy of the numerical method was validated by comparing representative simulations under different numerical conditions. The computation of the exchange step by the Runge-Kutta method was validated by comparison to the results provided by the stiff ODE solver RADAU; solutions computed by Runge-Kutta and RADAU were identical within 0.1%. Increasing the number of axial segments provides tighter coupling between the exchange and convective steps and reduces the artificial axial mixing introduced by the last step of the algorithm (Fig. 4D). The number of axial segments needed to produce accurate results depended on the type of data to be fit. A single-segment model was sufficient to accurately predict lymph-to-plasma ratios, whereas osmotic transient and indicator dilution studies required accounting for axial concentration gradients in the capillaries. However, only relatively coarse segmentation is necessary for osmotic transient simulations; 7 axial segments provide solutions for osmotic transients accurate to within 0.005% compared with 20 segments. Doubling the number of axial segments doubles the number of radial transfers and halves the model time step, so computational time is approximately proportional to N_{seg}^2.

Results

Model parameter values

Model simulations were used to predict the steady-state distribution of fluid exchange across the capillary wall and were compared with experimental data from lymph sampling, multiple-indicator dilution (MID), and osmotic transient experiments in whole hearts. Parameter values were chosen to match the specific experimental conditions where possible, but typical values (listed in Table 1) obtained from other sources were used when specific information for a given study was not available. The transport parameters r_{sp}, $A_{sp}/S\Delta r$, and $L_{p,endo}$ were obtained by fitting the model to osmotic weight transient data collected in the Ringer-perfused rabbit heart (38); r_{lp} and $A_{lp}/S\Delta r$ were chosen to fit the C_L/C_p data of Laine and Granger (41).

Steady-state fluid exchange

Because our model conserves volume, steady-state net filtration from capillaries to interstitium is equal to the rate of lymph formation. Despite the large pore system's relatively low hydraulic conductivity, ~90% of the total steady-state filtration occurs through this system, because the low reflection coefficient of plasma proteins through the large pores prevents the development of a capillary osmotic pressure that can counterbalance the hydrostatic pressure difference driving filtration. In the steady state, lower capillary hydrostatic pressures at the venous end of the exchange unit are partially balanced by decreased interstitial fluid pressures and increased interstitial osmotic pressures exerted by components of the interstitial matrix. Net filtration, therefore, declines toward the venous end (Fig. 5), but it occurs at all positions in the exchange unit because lymph formation is distributed throughout the interstitial space and interstitial fluid pressure is higher than venous outflow pressure. The remainder of the transcapillary filtration occurs through the small pores, while flux across the endothelial cells is near zero and varies between filtration at upstream regions and readsorption at downstream capillary regions.

Lymph studies

Net flux of solute from capillary to interstitium must also balance the quantity drained away by the lymphatics in steady state. The transcapillary concentration ratio approaches 1 for solutes with high diffusive permeability compared with convective transport (low Péclet number) and falls to $1 - \sigma$ for exchange dominated by convection, assuming that the capillary wall acts as a single-path semipermeable barrier to exchange. This fact has been exploited to measure the selectivity of the capillary wall, with lymph-to-plasma concentration ratio (C_L/C_p) commonly used as an approximation of capillary filtrate-to-plasma concentration ratio.

A model prediction of C_L/C_p as a function of molecular size (Fig. 6) was generated for baseline conditions by matching fixed model parameters to the protocol of Laine and Granger (41). However, C_L/C_p values are of little use unless they are obtained at high enough filtration rates to ensure that the limit of $1 - \sigma$ is reached or lymph formation rates are measured simultaneously and used to correct for diffusive flux. Experimental data are particularly lacking in the heart, because multiple venous outlets into the right ventricle limit experimental interventions to raise venous pressure, the usual mechanism of increasing lymph flows. Pilati (51) is the only investigator to achieve filtration rate independence for solutes as small as albumin, but he required infusion of adenosine in addition to coronary sinus occlusion to produce this effect. Pilati's data are well fitted by the lower limit of C_L/C_p produced by the model by both increasing the venous pressure and lowering the lymph back pressure until approximately constant values of C_L/C_p were obtained. Under normal control conditions, model C_L/C_p values are significantly higher, in rough agreement with most of

the published observations. The series of Arturson et al. (4) shows an unrealistic flattening out of C_L/C_p vs. r_p, probably because dextrans are long strands that reptate through narrow passages head on and additional molecular length does not significantly increase their resistance to transcapillary exchange.

The model fits can be greatly improved when model parameters, including the venous outflow pressure and lymph conductance, can be matched to the experimental conditions. The parameters for transcapillary exchange were optimized by comparing simulated lymph flow, interstitial pressure, and albumin and β-lipoprotein concentrations with data taken from Laine and Granger (41) (Fig. 7). In these experiments, the capillary filtration rate was elevated by raising venous pressure, which in turn increased the hydrostatic driving force for fluid filtration out of the capillaries. Under these conditions, the interstitium gained volume until increasing mechanical forces in the tissue raised interstitial pressure to balance capillary pressure, resulting in a new steady state at a higher filtration rate, and lowered C_L/C_p for albumin and β-lipoprotein. Model steady-state filtration rates and interstitial pressures at given venous pressures closely matched the experimental data, although some experimentally observed plateauing of interstitial pressures at high venous pressure is not shown by the model because a linear approximation to the interstitial pressure-volume relationship has been used.

Multiple-indicator dilution studies

Solute permeability in whole organs can be measured by the MID technique. In the simplest type of MID experiment, inflow and outflow concentration time courses are measured as a bolus containing two tracer solutes passed through an organ. One solute, for example, albumin, is restricted to the vascular space and provides a measurement of the distribution of transit times through the organ; the other, for example, L-glucose, is permeant and enters the interstitial space, resulting in a lower and broader peak relative to the vascular reference. Models ranging in complexity from the simple Crone (18) expression to physiologically detailed models like MMID4 (9) can then be fit to extracellular tracer data to estimate a lumped solute conductance: the permeability-surface area product, *PS*. However, all previously described models assume purely diffusive solute exchange across the capillary wall.

The L-glucose indicator dilution data of Kuikka et al. (Ref. 40,Fig. 8) was fit with a concentration input function obtained by deconvolution of the albumin reference curve and optimized by varying only $A_{sp}/S\Delta r$. Under these conditions, $A_{sp}/S\Delta r$ is proportional to *PS* determined from the tracer flux. The optimized value of $A_{sp}/S\Delta r$ for the data set shown in Fig. 8 translated into a *PS* of 1.1 $ml\cdot s^{-1}\cdot g^{-1}$, identical to the value obtained in the original paper (40) with a model specialized for tracer transient analysis (MMID4). Model predictions were also validated against a specialized model (MMID4) for tracer exchange kinetics (9) and found to reproduce that specialized model's concentration outflow waveforms to within 0.01% over a range of *PS* values.

Extensive data, summarized in Fig. 9, show that solute permeabilities as measured by MID are roughly proportional to free diffusion coefficients for hydrophilic solutes smaller than inulin, although charge effects may also play a role in ion exchange. This observation implies a lack of relative restriction among this group of solutes, so any aqueous pores must be large compared with the solutes. Model predictions were generated for an ideal spherical solute obeying the Stokes-Einstein equation: $r_s = RT/N_A 6\pi\eta D$, where R is the gas constant and T is absolute temperature, in water at 37°C. L-Glucose and the other solutes shown in Fig. 9 are markedly hydrophilic and therefore are limited to the extracellular space. Note that there is an approximately twofold increase in solute permeability for Ringer-perfused hearts compared with blood-perfused preparations. We have used two values of $A_{sp}/S\Delta r$, 4.5

cm and 2.5 cm, to account for this disparity. For technical reasons, all reported C_L/C_p data in the heart have been obtained from blood-perfused preparations whereas osmotic transient experiments have relied exclusively on the Ringer-perfused preparation. It was also necessary to vary the small-pore radius from 9 to 5 nm in Ringer- and blood-perfused data sets to provide good fits to all data sets. The model parameterizations for the large-pore and endothelial transcellular pathways remain constant in all simulations.

Osmotic transient experiments

Figure 10 shows a representative fit to osmotic transient experiments in an isolated rabbit heart. In this experiment, the interstitium has gained a large quantity of water before the transient because of low (1 g/l) levels of albumin in the perfusate and the vascular resistance has been reduced by perfusion with papaverine, requiring modifications in the basic parameter set. After a step change in perfusate osmolarity using 20 mM NaCl, there is an initial rapid loss of water from the interstitium and cells to the plasma as osmotic equilibrium is restored. This is followed by a slower phase where the solute enters the interstitium to partially dissipate its transcapillary concentration gradient and mechanical elastic and secondary osmotic forces act to partially restore interstitial volume. A steady-state interstitial-to-plasma concentration ratio is achieved when the rate of solute entry into the interstitium is equal to the rate of removal by lymph. The time course of weight change is substantially different for larger solutes like albumin. Because only 0.5 mM albumin was used, the initial rate of weight loss is less than for NaCl, despite albumin's higher reflection coefficient. However, the duration of the weight transient is longer because transcapillary concentration gradients persist as the test solute penetrates the interstitium only very slowly.

Discussion

The model presented here has a number of features that allow it to realistically simulate fluid and solute exchange under a variety of experimental conditions. The most significant advances are the use of an axially distributed blood-tissue exchange (BTEX) region, inclusion of a lymphatic drain in the interstitium, and the independent computation of transcapillary solute and solvent fluxes through three different pathways.

Geometry of the BTEX region

Accurate simulations of osmotic transient and MID data can only be achieved by an axially distributed BTEX region. Our results show that compartmental models, which by definition impose a uniform capillary solute concentration, always underestimate σ during an osmotic transient experiment because the influx of solute-free water into upstream capillary regions dilutes solute in downstream regions (38). Well-mixed compartments, even in interstitial and parenchymal regions, are also inadequate for analyzing indicator dilution curves because they imply an infinite diffusion coefficient. Coupling a compartmental interstitium to an axially distributed capillary model would lead to solute leaving upstream regions of the capillary on one model time step and then reentering downstream regions ahead of the convective front on the next time step, preventing an accurate reproduction of the postcapillary concentration waveform.

In the long and narrow BTEX regions of cardiac tissue, radial exchange and axial convection in capillaries are rapid compared with axial transport times in interstitium and neglecting axial diffusive and convective fluxes is an appropriate approximation. The intracapillary transient time (~0.75 s) and the radial diffusive relaxation times are both several orders of magnitude faster than the axial diffusive relaxation time. The radial diffusional relaxation time for albumin, with an estimated interstitial diffusion coefficient of 1×10^{-7} cm^2/s, or 10% of its value in free solution (5) based on a capillary-to-myocyte

spacing of 2 μm, is ~0.2 s for mixing in the region adjacent to the capillary and ~3.2 s for complete radial interstitial relaxation with a half-intercapillary distance of 8 μm. The axial diffusive relaxation time in a 639-μm BTEX region would be almost 6 h. Axial gradients in the interstitium and cellular regions are therefore modest. Three-dimensional convective and diffusive fluxes of water and solutes in the interstitium have been modeled by Taylor et al. (62) and Levick (43), but application of these models in practical settings has been limited because measurements of interstitial hydraulic resistances, diffusion coefficients, and sieving coefficients are technically difficult to obtain.

The use of uniform hexagonal Krogh cylinders to describe BTEX geometry is reasonable in cardiac tissue. The approach assumes that solute entry into adjacent capillaries is synchronous and perfusate velocities are the same so that there is no net exchange among adjacent units. Although it is known that staggering of parallel capillaries and cross-connections between adjacent capillaries increases transport efficiency beyond that predicted by the Krogh model (13,36), these anatomic features are most relevant for highly diffusible flow-limited solutes like O_2 and CO_2, which are not coupled to fluid exchange. We also assume that transport properties remain uniform along the length of the capillary and that all exchange occurs in a well-defined bed of parallel capillaries. In reality, there is no clear-cut distinct division between exchange and transport vessels; the venular ends of capillaries may have higher permeabilities in some vascular beds (68). However, an alternative form of the model in which the large pores were localized to the downstream end of the capillary segment did not substantially affect the model fits to data presented in this paper.

Flow varies among exchange units in a whole organ, and flow heterogeneity within a vascular bed can influence transport, particularly for highly diffusible solutes like water, O_2, and CO_2 (13,39). Heterogeneity effects have been successfully modeled by splitting the capillary flow among a number of parallel pathways. For the data set given in Fig. 8, a multicapillary tracer model gave an estimated *PS* 21% greater than the value obtained by neglecting flow heterogeneity (40). We have ignored flow heterogeneity because the time course of bulk fluid and hydrophilic solute exchange is much slower than tracer water and gas exchange, so the dispersion introduced by flow heterogeneity is less important for osmotic transient and lymph studies. Seale and Harris (57) found that estimated parameter values varied by < 10% between homogeneous and heterogeneous flow models in experiments on osmotically driven water exchange in the lung.

Lymph formation

Inclusion of a lymphatic drain is necessary to achieve the correct steady-state distribution of material across the capillary wall. A model by Grabowski and Bassingthwaighte (27) that neglected the role of the lymphatics had a steady state with no net fluid flux across the capillary wall. Consequently, all solutes eventually diffused to a uniform concentration in plasma and interstitial fluid, a model prediction incompatible with observed lymph-to-plasma concentration ratios. This assumption also led the authors to incorrectly predict that the mechanical elasticity of the tissue would eventually force the interstitium to return to its original volume after a plasma osmolarity change, because it forced their model to a unique interstitial equilibrium volume independent of plasma osmolarity. However, our model shows that an increased plasma osmolarity leads to a new steady state at a lower J_v, V_{isf}, and p_{isf} after the transient transcapillary concentration difference dissipates.

The simple empirical model of lymph formation represented by Eqs. 35 and 36 approximates complex three-dimensional flows of water and solutes from interstitium to terminal lymphatics by a distributed consumption of interstitial fluid driven by a single hydrostatic pressure difference across a uniform lumped hydraulic resistance. The actual mechanism of lymph formation is more complex and most likely depends on rhythmic tissue

motion to fill terminal lymphatics through gaps free of junction strands between lymphatic endothelial cells, which act as one-way valves (55). Because lymphatic endothelial cells lack the surface glycocalyx and tight junction strand proteins that could lead to restriction of solutes and development of an osmotic pressure difference, our empirical formulation is consistent with this mechanism on time scales that are long compared with the heart rate. The approach presumes that myocardial contractility and heart rate remain constant over the course of a simulation, because it is well established that cyclic muscular contraction augments lymph flow, which would change the effective K_L. Accounting for the relationships among fluid gain, myocardial force development, and lymph formation is beyond the scope of this study.

Large solutes are excluded from an appreciable fraction of the interstitial volume by components of the interstitial matrix, which raises their activity in the remainder of the solution. The extravascular volume available to albumin, for example, has been estimated at ~62% of interstitial fluid in cardiac tissue (60), less than our prediction of $\gamma = 0.78$ from Eq. 32, probably because negative charges on both albumin and matrix proteins cause a greater exclusion than would be expected based on size alone. Solute-free interstitial water is likely closely associated with components of the interstitial matrix, whereas lymph is likely composed primarily of more free-flowing fluid. Therefore, true capillary filtrate concentrations rather than bulk interstitial concentrations were used to estimate lymph concentrations in the model.

Multiple-pathway models for transcapillary exchange

Our modeling suggests that the interplay among different pathways across the capillary wall is at least as important to understanding the transcapillary exchange processes as a detailed understanding of the mechanics of exchange through each pathway. Understanding how the proportions of J_v among the pathways change during an intervention is necessary to properly interpret experimental data and is particularly important during osmotic weight transient studies because the equivalent single-path phenomenological model is dependent on the relative magnitudes of J_v in each pathway (53) and this quantity changes over the course of the experiment.

Unlike osmotic transient experiments, measurements of σ based on C_L/C_p are typically obtained by proportionally increasing J_v through all pathways by hydrostatic pressure changes. Because increases in capillary hydrostatic pressure would cause increased fluid filtration and convective solute exchange through even the largest pores, a lower estimate of σ will be obtained by lymph analysis than osmotic transient methods if a multipath model is not used. There is some evidence of higher reflection coefficients for large solutes measured with the osmotic transient technique compared with C_L/C_p analysis; $\sigma_{albumin}$ was only 0.59 by Pilati's (51) measurement of filtration rate-independent C_L/C_p. However, a more careful comparison of the two techniques in the same experimental system is needed to make definite conclusions.

Morphological basis for transcapillary pathways

Osmotic transient, lymphatic, and indicator dilution data sets are all consistent with a three-pathway description of capillary wall morphology. The small-pore pathway likely corresponds to the periendothelial cleft. We have used the simple classic small- and large-pore approach in this paper for simplicity, which places the steric hindrance at the cleft walls. Although straight-walled cylindrical pores are only a crude approximation of capillary wall morphology, the areas and radii used in simplified pore theories provide a rough correspondence to observable anatomy. Our model requires a small-pore radius of ~9 nm to provide some restriction to solutes the size of albumin ($\sigma = 0.45$ for this path) but at the

same time allow significant penetration of albumin into the interstitium by ~ 15 min into an osmotic transient. This estimate of small-pore width is larger than that obtained by other investigators using osmotic transient methods (14,27,49), but the fits to a complete albumin transient have never been reported and good fits to the initial slopes of the transients can be obtained with smaller pore sizes. Steady-state lymph-to-plasma concentration ratios, performed under blood perfusion, suggest a more restrictive 5-nm-radius pore. The fact that small-solute permeabilities vary by over a factor of 2 between blood- and Ringer-perfused preparations suggests that this is likely a consequence of real differences in capillary function between the preparations.

Detailed three-dimensional models of the capillary glycocalyx and cleft junction provide a more complete description of pericellular transport (34) but do not eliminate the need for multiple pathways. With fibers of 0.6-nm radius spaced ~7 nm apart, these models suggest that the capillary glycocalyx could provide restriction to solutes the size of albumin, but a transcellular pathway for water alone is still necessary to explain the large transient fluxes of solute-free water that leave the tissue in response to an acute increase in small-solute plasma concentration. Tracer labeling of the interendothelial clefts (25), observations of the endothelial junction morphology (2,15), and increases in capillary permeability following pronase digestion of glycocalyx (1,35) provide support for this view. Thinning of the glycocalyx under Ringer perfusion would also be interpreted as an increase in apparent small-pore area and radius.

A large, nonselective pore provides a transcapillary passage for even very large solutes, but its exact nature remains open to debate (46,53). Large pores could occur as junctions between three endothelial cells, vesicular transport, transport through fused vesicles, or infrequent gaps or thinning of the capillary glycocalyx. These are probably more frequent toward the venous end of capillaries as shown by the preferential escape of water-soluble dyes from the venous end of the microcirculation (68). However, an alternate form of our model in which the large pores were localized to the last axial segment of the BTEX unit gave model fits nearly identical to the distributed form. Developing a detailed mechanistic model of large-pore structure is relatively unimportant, because these pores are large even compared with macromolecules.

The pathway exclusive to water exchange is likely through the endothelial plasmalemma, and the pathway is at least partly mediated by the aquaporin-1 water channels present on cardiac endothelial cells (32,66). Recent experiments have shown that mercurials, known inhibitors of aquaporin-1, inhibit osmotically induced water exchange across the renal vasa recta and pulmonary capillaries (16,23,47). The effect is most evident for small solutes like NaCl and sucrose, likely because small solutes exert significant osmotic pressure across only the water-exclusive aquaporin channels. Larger solutes like albumin induce fluid movements even in the presence of aquaporin-blocking agents because they have a significant reflection coefficient for paracellular exchange. These results are qualitatively consistent with our three-pathway description of transcapillary fluid exchange, but quantitative comparisons of model and experiment are problematic because the toxicity of mercury makes well-controlled experiments under physiological normal conditions difficult.

In conclusion, the biggest barrier to large-scale physiological model development is the scarcity of readily available high-quality data obtained under precisely defined experimental conditions. As models grow more complex and require multiple experimental methodologies for validation, systematic databasing will be needed to provide fuel for development. However, once developed, a model becomes a powerful tool for uniting disparate observations into a common theoretical framework.

The key contribution of the model we have presented is its ability to integrate several distinct sets of experimental data into a single self-consistent theoretical framework. Detailed models of tracer kinetics in whole organs are already in widespread use for the analysis of tracer-transient data. These models are computationally faster and a better choice for the practical analysis of MID experiments because they include phenomena that are ignored by our model such as flow heterogeneity and the uptake and metabolism of substrates by cells. However, a fundamental assumption made by these types of models is that bulk fluid exchange is negligible, which clearly precludes their application to osmotic transient and lymph sampling techniques. Likewise, the steady-state sampling of lymph fluid does not require an elaborate kinetic model; current analysis techniques are adequate to explain most observations. However, analysis methods based on a steady-state assumption are fundamentally unsuited for application to understanding transient kinetic behaviors. It is in the osmotic transient experiment, in which a severe perturbation to the system causes large and transient bulk fluid flows, that the model presented in this paper has its greatest utility. The analysis of osmotic transient data sets, resulting in the estimation of parameters used in this paper, is the subject of the companion paper (38).

Acknowledgments

The authors thank Dr. Fernando Vargas for critical review of the manuscript.

Disclosures: This work was supported by National Institutes of Health National Center for Research Resources Grant 5-P41-RR-1243. M. Kellen was supported by a National Heart, Lung, and Blood Institute training grant in cardiovascular bioengineering (HL-07403-24).

References

1. Adamson RH. Permeability of frog mesenteric capillaries after partial pronase digestion of the endothelial glycocalyx. J Physiol. 1990; 428:1–13. [PubMed: 2231409]
2. Adamson RH, Clough G. Plasma proteins modify the endothelial cell glycocalyx of frog mesenteric microvessels. J Physiol. 1992; 445:473–486. [PubMed: 1501143]
3. Alvarez OA, Yudilevich DL. Heart capillary permeability to lipid-insoluble molecules. J Physiol. 1969; 202:45–58. [PubMed: 5770913]
4. Arturson G, Areskog NH, Arfors K, Grotte G, Malmberg P. The transport of macromolecules across the blood-lymph barrier. Influence of capillary pressure on macromolecular composition of lymph. Bibl Anat. 1969; 10:228–233. [PubMed: 5407368]
5. Aukland K, Reed RK. Interstitial-lymphatic mechanisms in the control of extracellular fluid volume. Physiol Rev. 1993; 73:1–78. [PubMed: 8419962]
6. Bassingthwaighte JB. A concurrent flow model for extraction during transcapillary passage. Circ Res. 1974; 35:483–503. [PubMed: 4608628]
7. Bassingthwaighte, JB. The myocardial cell. In: Brandenberg, RO.; Fuster, V.; Giuliani, ER.; Mcgoon, DC., editors. Cardiology: Fundamentals and Practice. Chicago, IL: Year Book Medical; 1987. p. 113-149.
8. Bassingthwaighte, JB.; Knopp, TJ.; Hazelrig, JB. A concurrent flow model for capillary-tissue exchanges. In: Crone, C.; Lassen, NA., editors. Capillary Permeability: The Transfer of Molecules and Ions from Capillary Blood and Tissue. Copenhagen: Munksgaard; 1970. p. 60-80.
9. Bassingthwaighte JB, Wang CY, Chan IS. Blood-tissue exchange via transport and transformation by capillary endothelial cells. Circ Res. 1989; 65:997–1020. [PubMed: 2791233]
10. Bassingthwaighte JB, Yipintsoi T, Grabowski EF. Myocardial capillary permeability: hydrophilic solutes penetrate 100 Å clefts. Bibl Anat. 1975; 13:24–27. [PubMed: 1231735]
11. Batra S, Rakusan K. Morphometric analysis of capillary nets in rat myocardium. Adv Exp Med Biol. 1990; 277:261–270.
12. Bean, CP. The physics of porous membranes—neutral pores. In: Einsenman, G., editor. Membranes: Macroscopic Systems and Models. New York: Dekker; 1972. p. 1-54.

13. Beard DA, Bassingthwaighte JB. Advection and diffusion of substances in biological tissues with complex vascular networks. Ann Biomed Eng. 2000; 28:253–268. [PubMed: 10784090]
14. Bloom G, Johnson JA. A model for osmotically induced weight transient in the isolated rabbit heart. Microvasc Res. 1981; 22:64–79. [PubMed: 7278701]
15. Bundgaard M. The three-dimensional organization of tight junctions in a capillary endothelium revealed by serial-section electron microscopy. J Ultrastruct Res. 1984; 88:1–17. [PubMed: 6545375]
16. Carter EP, Olveczky BP, Matthay MA, Verkman AS. High microvascular endothelial water permeability in mouse lung measured by a pleural surface fluorescence method. Biophys J. 1998; 74:2121–2128. [PubMed: 9545071]
17. Chilian, WM.; Layne, SM.; Nellis, SH. Microvascular pressure profiles in the left and right coronary circulations. In: Kajiya, F.; Klassen, GA.; Spaan, JAE.; Hoffman, JIE., editors. Coronary Circulation: Basic Mechanisms and Clinical Relevance. Tokyo: Springer; 1990.
18. Crone C. The permeability of capillaries in various organs as determined by the use of the “indicator diffusion” method. Acta Physiol Scand. 1963; 58:292–305. [PubMed: 14078649]
19. Curry FE. A hydrodynamic description of the osmotic reflection coefficient with application to the pore theory of transcapillary exchange. Microvasc Res. 1974; 8:236–252. [PubMed: 4437406]
20. Curry, FE. Handbook of Physiology. The Cardiovascular System. Microcirculation. Vol. IV. Bethesda, MD: Am Physiol Soc; 1984. Mechanics and thermodynamics of transcapillary exchange; p. 309-374.sect. 2chapt. 8
21. Curry FE, Mason JC, Michel CC. Osmotic reflexion coefficients of capillary walls to low molecular weight hydrophilic solutes measured in single perfused capillaries of the frog mesentery. J Physiol. 1976; 261:319–336. [PubMed: 1086361]
22. Effros RM. Osmotic extraction of hypotonic fluid from the lungs. J Clin Invest. 1974; 54:935–947. [PubMed: 4430723]
23. Effros RM, Darin C, Jacobs ER, Rogers RA, Krenz G, Schneeberger EE. Water transport and the distribution of aquaporin-1 in pulmonary air spaces. J Appl Physiol. 1997; 83:1002–1016. [PubMed: 9292489]
24. Feola M, Glick G. Cardiac lymph flow and composition in acute myocardial ischemia in dogs. Am J Physiol. 1975; 229:44–48. [PubMed: 238406]
25. Fu B, Curry FR, Adamson RH, Weinbaum S. A model for interpreting the tracer labeling of interendothelial clefts. Ann Biomed Eng. 1997; 25:375–397. [PubMed: 9084841]
26. Gonzalez F, Bassingthwaighte JB. Heterogeneities in regional volumes of distribution and flows in rabbit heart. Am J Physiol Heart Circ Physiol. 1990; 258:H1012–H1024.
27. Grabowski, EF.; Bassingthwaighte, JB. An osmotic weight transient model for estimation of capillary transport parameters in myocardium. In: Grayson, J.; Zingg, W., editors. Microcirculation (Proceedings of the First World Congress for the Microcirculation). Vol. 2. New York: Plenum; 1976. p. 29-50.
28. Guller G, Yipintsoi T, Orvis AL, Bassingthwaighte JB. Myocardial sodium extraction at varied coronary flows in the dog. Circ Res. 1975; 37:359–378. [PubMed: 1098804]
29. Hairer, E.; Nørsett, SP.; Wanner, G. Solving Ordinary Differential Equations I. Nonstiff Problems. New York: Springer; 1993.
30. Hairer, E.; Wanner, G. Solving Ordinary Differential Equations II. Stiff and Differential Algebraic Problems. New York: Springer; 1996.
31. Harris TR, Gervin CA, Burks D, Custer P. Effects of coronary flow reduction on capillary-myocardial exchange in dogs. Am J Physiol Heart Circ Physiol. 1978; 234:H679–H689.
32. Hasegawa H, Lian SC, Finkbeiner WE, Verkman AS. Extrarenal tissue distribution of CHIP28 water channels by in situ hybridization and antibody staining. Am J Physiol Cell Physiol. 1994; 266:C893–C903.
33. Haunsø S, Paaske WP, Sejrsen P, Amtorp O. Capillary permeability in canine myocardium as determined by bolus injection, residue detection. Acta Physiol Scand. 1980; 108:389–397. [PubMed: 6774595]
34. Hu X, Weinbaum S. A new view of Starling's hypothesis at the microstructural level. Microvasc Res. 1999; 58:281–304. [PubMed: 10527770]

35. Huxley VH, Williams DA. Role of a glycocalyx on coronary arteriole permeability to proteins: evidence from enzyme treatments. Am J Physiol Heart Circ Physiol. 2000; 278:H1177–H1185. [PubMed: 10749712]
36. Kassab GS, Berkley J, Fung YC. Analysis of pig's coronary arterial blood flow with detailed anatomical data. Ann Biomed Eng. 1997; 25:204–217. [PubMed: 9124734]
37. Kedem O, Katchalsky A. Thermodynamic analysis of the permeability of biological membranes to non-electrolytes. Biochim Biophys Acta. 1958; 27:229–246. [PubMed: 13522722]
38. Kellen MR, Bassingthwaighte JB. Transient transcapillary exchange of water driven by osmotic forces in the heart. Am J Physiol Heart Circ Physiol. 2003; 285:H1317–H1331. [PubMed: 12738617]
39. King RB, Raymond GM, Bassingthwaighte JB. Modeling blood flow heterogeneity. Ann Biomed Eng. 1996; 24:352–372. [PubMed: 8734057]
40. Kuikka J, Levin M, Bassingthwaighte JB. Multiple tracer dilution estimates of d- and 2-deoxy-d-glucose uptake by the heart. Am J Physiol Heart Circ Physiol. 1986; 250:H29–H42.
41. Laine GA, Granger HJ. Microvascular, interstitial, and lymphatic interactions in normal heart. Am J Physiol Heart Circ Physiol. 1985; 249:H834–H842.
42. Laughlin MH, Diana JN. Myocardial transcapillary exchange in the hypertrophied heart of the dog. Am J Physiol. 1975; 229:838–846. [PubMed: 129013]
43. Levick JR. An analysis of the interaction between interstitial plasma protein, interstitial flow, and fenestral filtration and its application to synovium. Microvasc Res. 1994; 47:90–125. [PubMed: 8022316]
44. Lightfoot EN, Bassingthwaighte JB, Grabowski EF. Hydrodynamic models for diffusion in microporous membranes. Ann Biomed Eng. 1976; 4:78–90. [PubMed: 937776]
45. Mann GE. Alterations of myocardial capillary permeability by albumin in the isolated, perfused rabbit heart. J Physiol. 1981; 319:311–323. [PubMed: 6798198]
46. Michel CC, Curry FE. Microvascular permeability. Physiol Rev. 1999; 79:703–761. [PubMed: 10390517]
47. Pallone TL, Kishore BK, Nielsen S, Agre P, Knepper MA. Evidence that aquaporin-1 mediates NaCl-induced water flux across descending vasa recta. Am J Physiol Renal Physiol. 1997; 272:F587–F596.
48. Pappenheimer JR. Passage of molecules through capillary walls. Physiol Rev. 1953; 33:387–423. [PubMed: 13088295]
49. Pappenheimer JR, Renkin EM, Borrero LM. Filtration, diffusion, and molecular sieving through peripheral capillary membranes. Am J Physiol. 1951; 167:13–46. [PubMed: 14885465]
50. Patlak CS, Goldstein DA, Hoffman JF. The flow of solute and solvent across a two-membrane system. J Theor Biol. 1963; 5:426–442. [PubMed: 5875168]
51. Pilati CF. Macromolecular transport in canine coronary microvasculature. Am J Physiol Heart Circ Physiol. 1990; 258:H748–H753.
52. Renkin EM. Transport of potassium-42 from blood to tissue in isolated mammalian skeletal muscle. Am J Physiol. 1959; 197:1205–1210. [PubMed: 14437359]

52a. Renkin EM, Watson PD, Sloop CH, Joyner WM, Curry FE. Transport pathways for fluid and large molecules in microvascular endothelium of the dog's paw. Microvasc Res. 1977; 14:205–214. [PubMed: 927218]

53. Rippe B, Haraldsson B. Transport of macromolecules across microvascular walls: the two-pore theory. Physiol Rev. 1994; 74:163–219. [PubMed: 8295933]
54. Rose CP, Goresky CA. Vasomoter control of capillary transit time heterogeneity on the canine coronary circulation. Circ Res. 1976; 39:541–544. [PubMed: 786495]
55. Schmid-Schönbein, GW.; Ikomi, F. Biomechanics of lymph transport. In: Jaffrin, MY.; Caro, C., editors. Biological Flows. New York: Plenum; 1995. p. 353-360.
56. Schwartz LM, Bukowski TR, Revkin JH, Bassingthwaighte JB. Cardiac endothelial transport and metabolism of adenosine and inosine. Am J Physiol Heart Circ Physiol. 1999; 277:H1241–H1251.
57. Seale KT, Harris TR. A three-compartment model of osmotic water exchange in the lung microvasculature. Ann Biomed Eng. 2000; 28:1019–1027. [PubMed: 11144663]

58. Shaw M. Exclusion in hyaluronate gels. Biophys J. 1977; 17:47–55. [PubMed: 831856]
59. Sipkema P, Takkenberg JJM, Zeeuwe PEM, Westerhof N. Left coronary pressure-flow relations of the beating and arrested rabbit heart at different ventricular volumes. Cardiovasc Res. 1998; 40:88–95. [PubMed: 9876320]
60. Sunnergren KP. The effects of hyaluronidase on interstitial hydration, plasma protein exclusion, and microvascular permeability in the isolated perfused rat heart. Circ Res. 1985; 30:286–297.
61. Tanford, C. Physical Chemistry of Macromolecules. New York: Wiley; 1961.
62. Taylor DG, Bert JL, Bowen BD. A mathematical model of interstitial transport. I. Theory. Microvasc Res. 1990; 39:253–278. [PubMed: 2194091]
63. Ullal SR, Kluge TH, Kerth WJ, Gerbode F. Flow and composition of cardiac lymph in dogs. Ann Surg. 1972; 175:299–304. [PubMed: 5077793]
64. Vargas FF, Blackshear GL. Secondary driving forces affecting transcapillary osmotic flows in perfused heart. Am J Physiol Heart Circ Physiol. 1981; 240:H457–H464.
65. Vargas F, Johnson JA. An estimate of reflection coefficients for rabbit heart capillaries. J Gen Physiol. 1964; 47:667–677. [PubMed: 14127605]
66. Verkman AS, Van Hoek AN, Ma T, Frigeri A, Skach WR, Mitra A, Tamarappoo BK, Farinas J. Water transport across mammalian cell membranes. Am J Physiol Cell Physiol. 1996; 270:C12–C30.
67. Weast, RC. CRC Handbook of Chemistry and Physics. Boca Raton, FL: CRC; 1979.
68. Wiederhielm CA. Transcapillary and interstitial transport phenomena in the mesentery. Fed Proc. 1966; 25:1789–1798. [PubMed: 5927414]
69. Wolf MB, Watson PD. Measurement of osmotic reflection coefficient for small molecules in cat hindlimbs. Am J Physiol Heart Circ Physiol. 1989; 256:H282–H290.
70. Ziegler WH, Goresky CA. Transcapillary exchange in the working left ventricle of the dog. Circ Res. 1971; 29:181–207. [PubMed: 4935840]

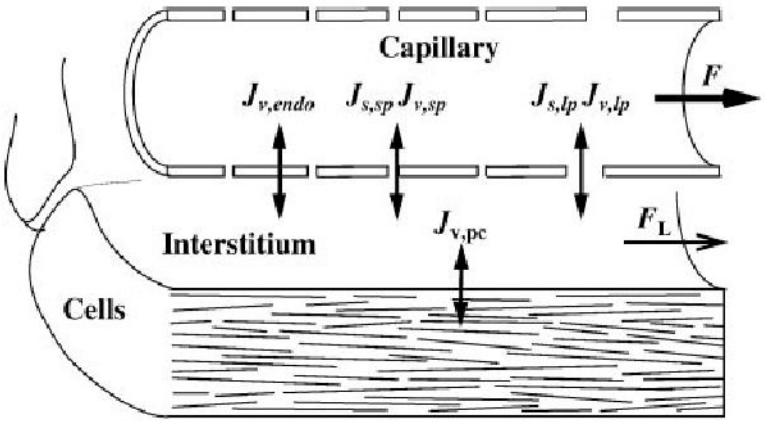

Fig. 1.

Mass transport in a blood-tissue exchange unit: axial flow through the capillary (F), transcapillary fluid flux (through 3 paths, $J_{v,k}$, calculated in Eq. 28) and solute flux (J_s, calculated in Eq. 42) through large (lp)- and small-pore (sp) pathways, fluid flux only across endothelial cells (J_v endo) and into parenchymal cells ($J_{v,pc}$, calculated in Eq. 34), and drainage of interstitial fluid by the lymphatics (F_L, calculated in Eq. 35).

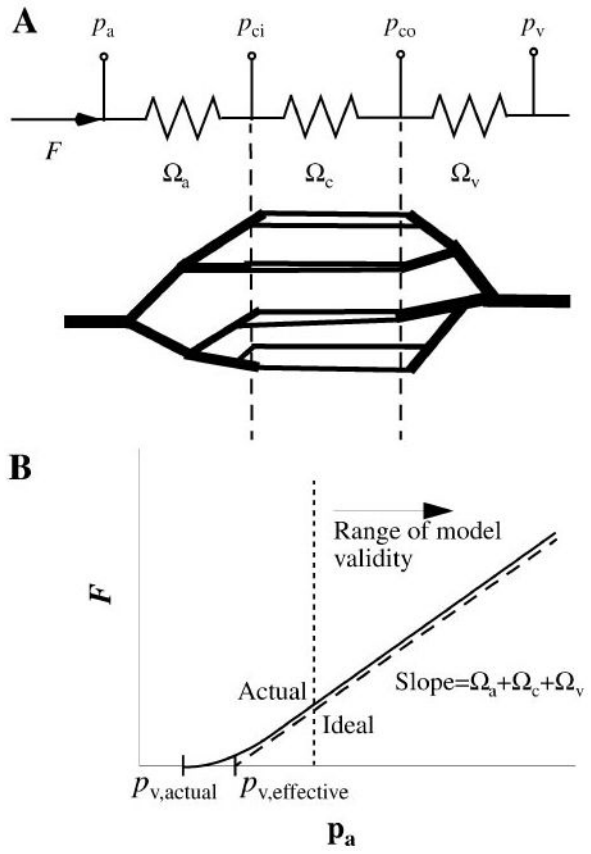

Fig. 2.

A: flow through a vascular network modeled as flow through 3 lumped resistances corresponding to arteries, capillaries, and veins. Electrical analog circuit is shown at *top*. *B*: at very low flows the observed pressure-flow relationship may deviate from linearity because of changing vascular volumes, but the slope is constant in the normal physiological range, even if the venous pressure ($p_{v,effective}$) does not match the actual zero-flow pressure ($p_{v,actual}$). P_a, P_v, arterial and venous permeabilities; Ω_a, Ω_c, Ω_v, arterial, capillary, and venous vascular resistances.

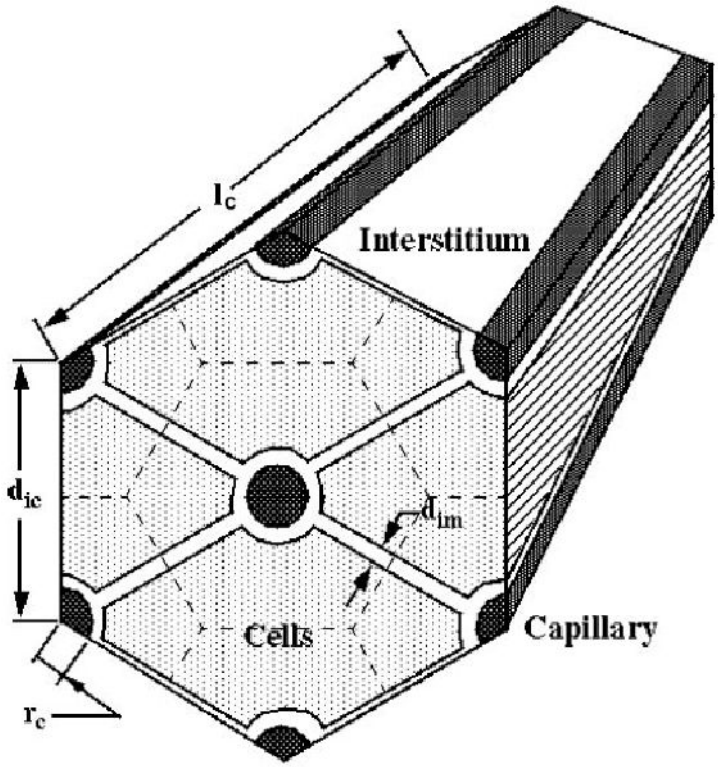

Fig. 3.

Cardiac tissue geometry is modeled with a hexagonal array of Krogh cylinders, with 1 capillary per blood-tissue exchange (BTEX) unit. Intercapillary distance d_{ic} = 19 μm, capillary radius r_c = 2.5 μm, intermyocyte spacing d_{im} = 1.8 μm, and capillary length l_c = 639 μm.

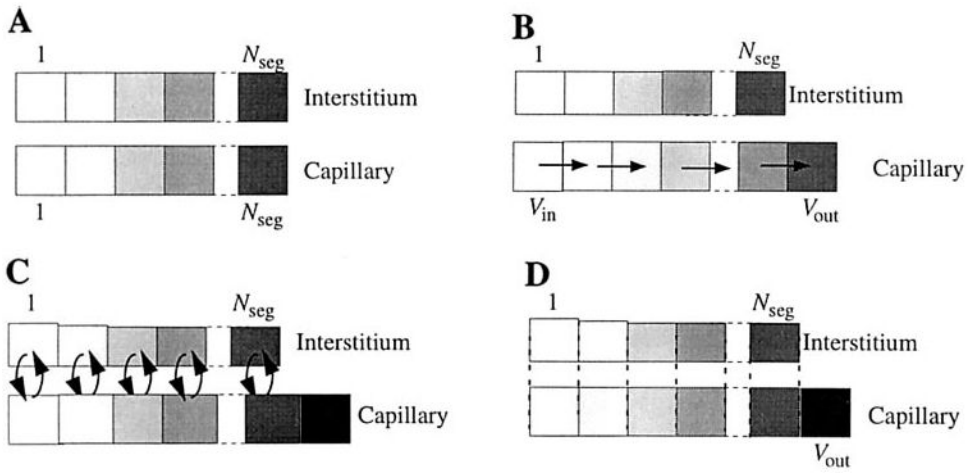

Fig. 4.

Outline of steps for numerical computation of model solutions at N_{seg} axial segments in capillary and interstitium. The cellular region is segmented in the same manner as the interstitial region, but is omitted from the figures for clarity. *A*: regions are initially divided into N_{seg} axial segments of equal volume. *B*: axial convection occurs with a time step chosen to match the time needed for fluid to move exactly 1 segment downstream. At each time step, the first capillary segment is filled with inflowing fluid (V_{in}), and the other segments are each displaced by one to the right, and the end segment slides to the outflow (V_{out}). *C*: radial fluid and solute exchange occurs among regions. Because the capillary is modeled as a constant volume, net volume influx into the capillary segments causes axial expansion, whereas net volume efflux from capillary to ISF causes axial shrinkage. *D*: the final operation with the time step is to recalculate the contents of the expanded or shrunken volumes associated with each capillary segment to match the contents to the original spatial grid; V_{out} is the outflow from the BTEX region during this time step.

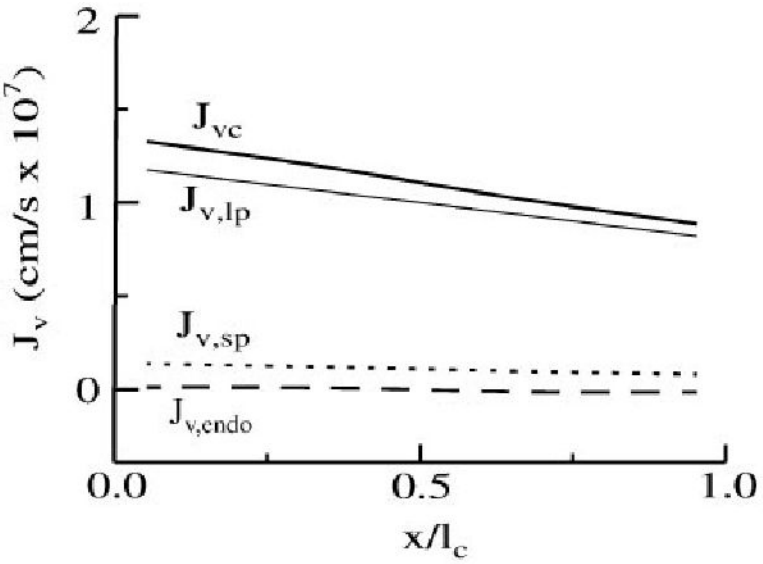

Fig. 5.
Steady-state volume flux (*Jv*) across the capillary wall for each pathway as a function of axial position within the BTEX unit.

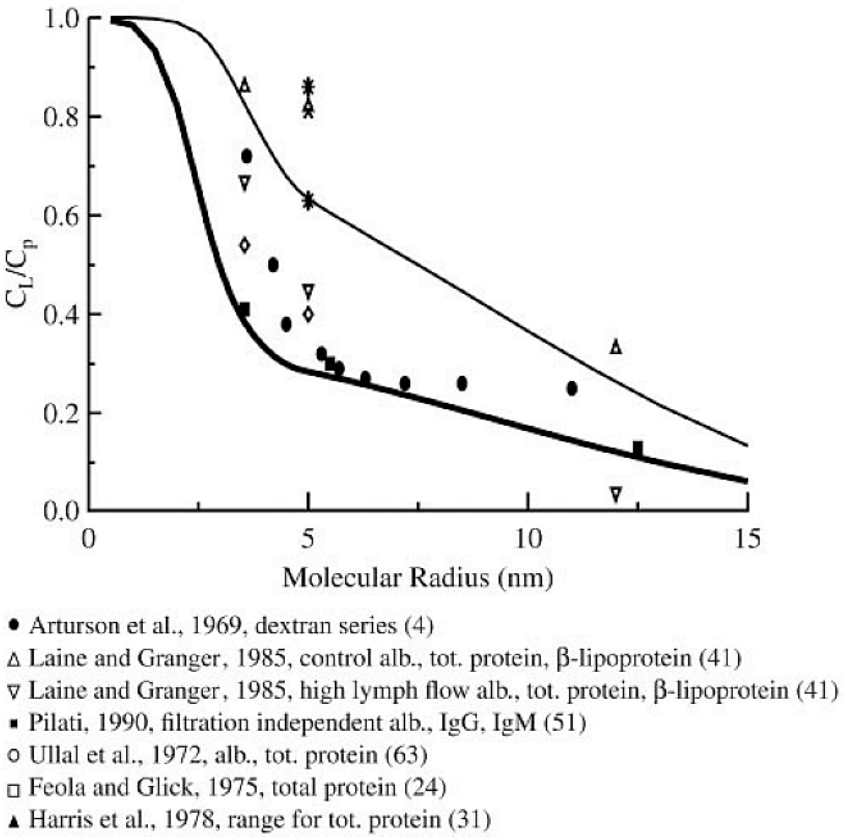

Fig. 6.

Steady-state lymph-to-plasma concentration ratio (C_L/C_p) values predicted by the model for control conditions (thin line) and at filtration rate independence (thick line) compared with a compilation of experimental data in mammalian cardiac tissue. Parameter values are from Table 1. *P*, σ, and γ are functions of molecular size and diffusion coefficient given by Eq. 32, 46, and 47; *D* was assumed proportional to $1/r_s$. Pilati's data are the most definitive; the other data were acquired and partially flow-limited conditions.

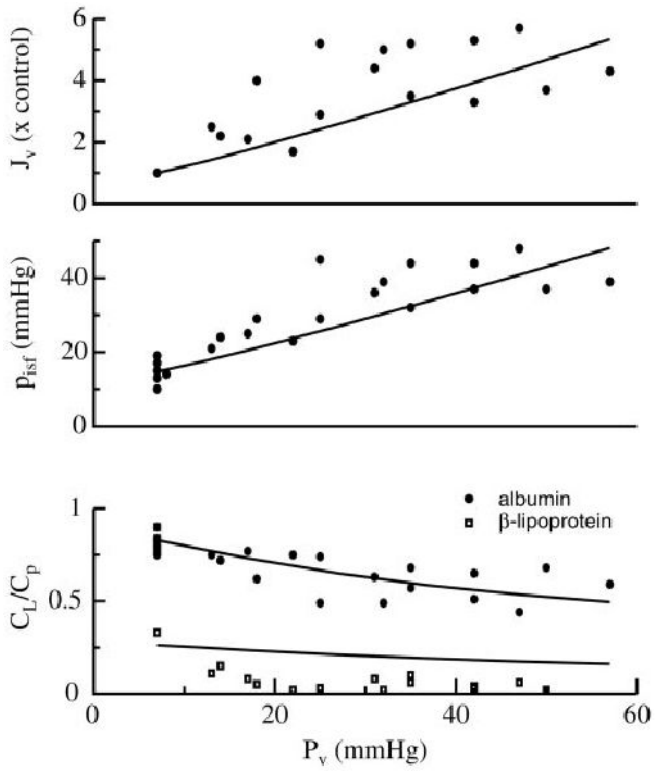

Fig. 7.

Simulated effect of changes in venous pressure (solid lines) at constant flow on the steady-state transcapillary filtration rate (J_v, *top*), interstitial pressure (p_{isf}, *middle*), and C_L/C_p (*bottom*) compared with data from dog heart (41).

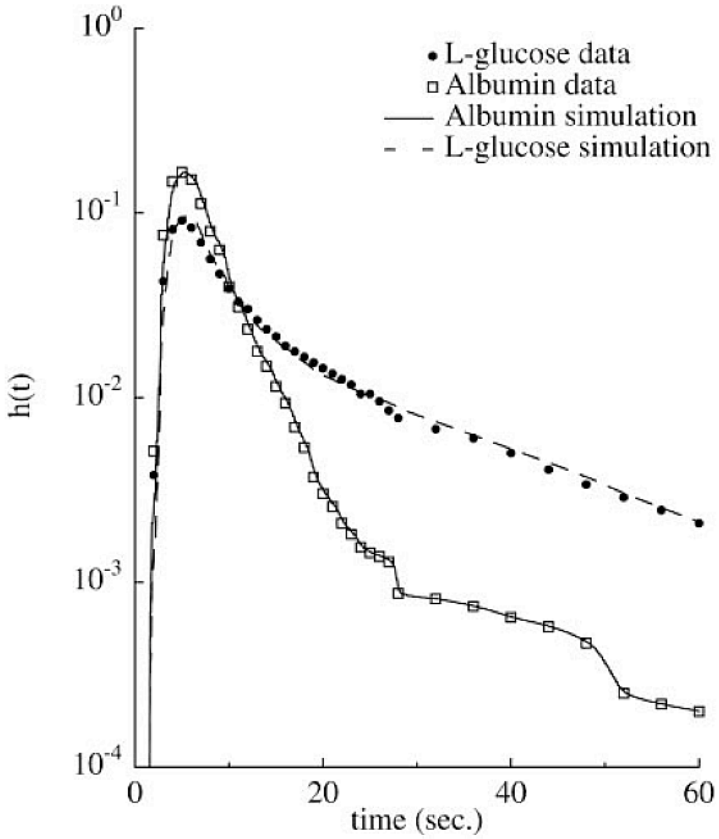

Fig. 8.

Model fit to multiple-indicator dilution data (data set 13078-1, Ref. 40). Data are normalized to give the transport function for passage through a BTEX unit [$h(t)$]. Model parameters taken from the paper are F = 1.7 ml·min^{-1}·g^{-1}, $\hat{V}_c$ = 0.035 ml/g, and $\hat{V}_{isf}$ = 0.28 ml/g.

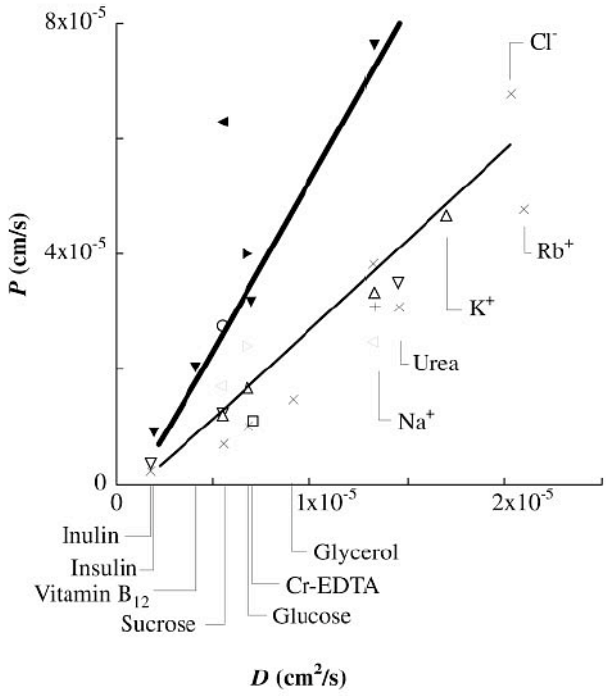

× Alvarez and Yudilevich, 1969 (3)
□ Haunsø et al., 1980 (33)
+ Guller et al., 1975 (28)
▽ Laughlin and Diana, 1975 (42)
△ Bassingthwaighte et al., 1975 (8)
○ Rose and Goresky, 1976 (54)
◁ Ziegler and Goresky, 1971 (70)
▼ Mann, 1981 (45)*
▷ Kuikka et al., 1986 (40)
► Kuikka et al., 1986 (40)*
◄ Schwartz et al., 2000 (56)*

Fig. 9.

Comparison of model permeability predictions for blood-perfused (thin line) and Ringer-perfused (thick line) preparations to experimental results from multiple-indicator dilution studies in mammalian cardiac tissue. Experimentally measured values of permeability-surface area product (*PS*) were converted to pure permeabilities by assuming a capillary surface area of 500 cm^2/g for comparison to values calculated by the model. Data sets taken from Ringer-perfused hearts are indicated by filled symbols and references marked with *. *D*, free diffusion coefficient.

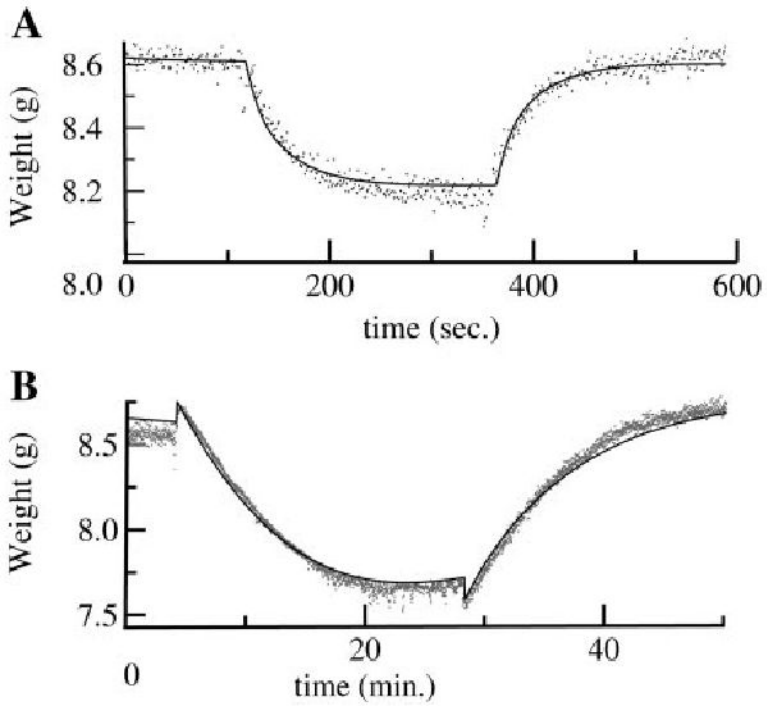

Fig. 10.

Model fit to osmotic transient data (38). The basic parameter set was adjusted by increasing d_{im} to 3 μm and decreasing collagen and interstitial matrix quantities (Q_{col} and Q_{im}) to 0.021 and 5.4×10^{-4} g/ml, respectively, to account for edema present in the experimental preparation. Flow was 13 ml/min, p_a was 24 mmHg, p_{isf} was 5.45 mmHg, and Ω_a was 1.33 mmHg·min·ml^{-1}. *A*: fit of model (solid line) to organ weight data with 20 mM NaCl as the osmotic agent. *B*: fit to transient in the same heart with 0.5 mM albumin as the osmotic agent. (The small sharp rise in weight at time = 4 min is due to the increased viscosity of the albumin-containing solution.)

Table 1

Terminology and parameter values

Symbol	Definition	Values	Units
A_{sp}/S_c	Small-pore fractional area	2.25×10^{-5} (Ringer perfused); 1.05×10^{-5} (blood perfused)	Dimensionless
A_{ip}/S_c	Large-pore fractional area	2.5×10^{-7}	Dimensionless
C	Concentration	$C^o_{NaCl}=150; C^o_{alb}=0.75$ (perfusate)	mM
d_{ic}	Distance between capillaries	d_{ic} = 18 (9)	μm
d_{im}	Distance between myocytes or between capillaries and myocytes	d_{im} = 1.8 (estimated from Ref. 26)	μm
D_j	Free diffusion coefficient of *j*th solute (at 37°C)	$D_{NaCl} = 2.0 \times 10^{-5}$ (67); $D_{suc} = 7.0 \times 10^{-6}$ (67); $D_{alb} = 9.1 \times 10^{-7}$ (61)	cm^2/s
E_n	*n*th Elastance coefficient (interstitium, cell)	E_1 = 15 mmHg (5); $E_2 = 0$, $E_3 = 0$	Variable
F	Flow through organ	28.8	ml/min
$\hat{F}$	Specific flow through organ	4.8	$ml \cdot min^{-1} \cdot g^{-1}$
F_L	Flow through lymphatics	0.22 (steady state)	ml/min
F(α)	Fractional reduction of *D* inside pore	$F(\alpha) = 1 - 2.104\alpha + 2.089\alpha^3 + \ldots$ (20)	Dimensionless
G(α)	Ratio of solute velocity to solvent velocity on the pore axis	$G(\alpha) = 1 - 0.667\alpha^2 - 0.1628\alpha^5$ (20)	Dimensionless
ISF or isf	Interstitial fluid		
$J_{S,j}$	Total net transcapillary solute flux of *j*th solute	$0–1.6 \times 10^{-9}$	$mol \cdot s^{-1} \cdot cm^{-2}$
$J_{V,k}$	Transcapillary volume flux through *k*th path	$0–1 \times 10^{-7}$	cm/s
$J_{V,endo}$	Transendothelial volume flux of pure water		
$J_{V,pc}$	Volume flux across parenchymal cell membrane	0 (steady state)	cm/s
$J_{L,s}$	Mass loss through lymphatics	3.2×10^{-5} (steady state)	mol/s
K_L	Lymphatic conductance	1×10^{-4} (41)	$ml \cdot s^{-1} \cdot mmHg^{-1} \cdot g^{-1}$
l_c	Capillary length	639 (11)	μm
$L_{p,sp}$	Small-pore hydraulic conductivity	1.3×10^{-8} (blood perfused); 8.8×10^{-8} (Ringer perfused)	$cm \cdot s^{-1} \cdot mmHg^{-1}$
$L_{p,lp}$	Large-pore hydraulic conductivity	6.8×10^{-9}	$cm \cdot s^{-1} \cdot mmHg^{-1}$
$L_{p,endo}$	Transendothelial cell hydraulic conductivity	1.4×10^{-8}	$cm \cdot s^{-1} \cdot mmHg^{-1}$
$L_{p,pc}$	Hydraulic conductivity across parenchymal cell membrane	1×10^{-9}	$cm \cdot s^{-1} \cdot mmHg^{-1}$
n	Quantity of solute	0–0.014	mol
N_c	Number of capillaries in whole organ	2.8×10^7	Dimensionless
$\hat{N_c}$	Capillary density	4.6×10^6	g^{-1}
N_{seg}	Number of axial segments in BTEX unit	7	Dimensionless
p	Pressure (arterial, capillary inlet, capillary outlet, venous, interstitial, lymphatic)	p_a = 87; p_{ci} = 16.9; p_{co} = 13.3; p_v = 7; p_{ist} = 13 (at steady state); $p_L = p_v$	mmHg
P_j	Permeability of *j*th solute (blood perfused or Ringer perfused)	$P_{NaCl} = 3.5 \times 10^{-5}$ or 8.1×10^{-5}; $P_{suc} = 1.0 \times 10^{-5}$ or 2.6×10^{-5}; $P_{alb} = 3.5 \times 10^{-7}$ or 4.3×10^{-7}	cm/s
Pe	Péclet number	0–2	Dimensionless

Symbol	Definition	Values	Units
Q	Quantity (interstitial matrix, collagen, parenchymal cell)	Q_{im} = 0.05 (5); Q_{col} = 0.0013 (5); Q_{pc} = 0.32	g/ml
r_c	Capillary radius	2.5 (9)	μm
r_f	Fiber radius (interstitial matrix, collagen)	$r_{f,im}$ = 0.3; $r_{f,col}$ = 4	nm
r_{sp}	Small-pore radius	9.0 (Ringer perfused); 5.0 (blood perfused)	nm
r_{lp}	Large-pore radius	23.5	nm
r_s	Solute radius	r_{NaCl} = 0.22; $r_{albumin}$ = 3.6; $r_{sucrose}$ = 0.45	nm
Δr	Capillary wall thickness	0.5	μm
R	Gas constant	8.314	$J \cdot mol^{-1} \cdot K^{-1}$
S	Surface area per BTEX unit (capillary, parenchymal cell)	$S_c = 1.00 \times 10^4$; $S_{pc} = 3.67 \times 10^4$	μm^2
$\hat{S}$	Specific surface area (capillary, parenchymal cell)	$\hat{S}_c$ = 487; $\hat{S}_{pc}$ = 1,780	cm^2/g
t	Time	Independent variable	s
T	Absolute temperature	310	°K
u	Perfusate velocity in capillary	0.075	cm/s
v	Anatomic volume (BTEX unit, capillary, interstitial, parenchymal cell)	$v_{btex} = 1.77 \times 10^5$; $v_c = 1.25 \times 10^4$; v_{isf} 4.44×10^4; $v_{pc} = 1.20 \times 10^5$	μm^3
V_f	Fluid volume (capillary, interstitial, parenchymal cell)	$V_{f,c} = 1.25 \times 10^4$; $V_{f,isf} = 4.30 \times 10^4$; $V_{f,pc} = 9.06 \times 10^4$	μm^3
V_s	Solid volume (capillary, interstitial, parenchymal cell)	$V_{s,c}$ = 0; $V_{s,isf} = 1.78 \times 10^3$; $V_{s.pc} = 2.99 \times 10^4$	μm^3
$\hat{V}$	Whole organ volume fraction (large vessels, capillaries, interstitium, parenchymal cells)	$\hat{V}_{lv}$ = 0.085; $\hat{V}_c$ = 0.064; $\hat{V}_{f,\,isf}$ = 0.226; $\hat{V}_{f,\,pc}$ = 0.462; $\hat{V}_{s,\,isf}$ = 0.009; $\hat{V}_{s,\,pc}$ = 0.154	Dimensionless
$\hat{V}$	Specific volume (large vessels, capillaries, interstitium, parenchymal cells)	$\hat{V}_{lv}$ = 0.080 (26); $\hat{V}_c$ = 0.060 (26); $\hat{V}_{f,\,isf}$ = 0.213 (26); $\hat{V}_{f,\,pc}$ = 0.436 (26); $\hat{V}_{s,\,isf}$ = 0.008 (26); $\hat{V}_{s,\,pc}$ = 0.146 (26)	ml/g
W	Organ weight	W^o = 6	g
x	Axial coordinate along capillary length	Independent variable	cm
α	Ratio of solute radius to pore radius	0–1	Dimensionless
γ	Fractional volume of distribution in interstitium (of a solute)	γ_{NaCl} = 0.99; γ_{suc} = 0.99; γ_{alb} = 0.78	Dimensionless
η	Perfusate viscosity (at 37°C)	0.007	$g \cdot cm^{-1} \cdot s^{-1}$
Π	Osmotic pressure	0–5,400	mmHg
ρ	Density (solid, fluid, organ)	ρ_s = 1.33 (7); ρ_f = 1.01 (67); ρ_{org} = 1.06 (7)	g/ml
σ	Reflection coefficient of *j*th solute through small pore (blood perfused or Ringer perfused), large pore, endothelial cell	NaCl: σ_{sp} = 0.01 or 0.00; σ_{lp} = 0.0; σ_{ec} = 1.0; sucrose: σ_{sp} = 0.03 or 0.01; σ_{lp} = 0.0; σ_{ec} = 1.0; albumin: σ_{sp} = 0.89 or 0.44; σ_{lp} = 0.07; σ_{ec} = 1.0	Dimensionless
ϕ_n	*n*th Virial coefficient	NaCl: ϕ_1 = 1.87; ϕ_2 = 0; ϕ_3 = 0 (67); sucrose: ϕ_1 = 1.0; ϕ_2 = 0; ϕ_3 = 0 (67); albumin: ϕ_1 = 0.92; ϕ_2 = 0.48; ϕ_3 = 0.30 (43)	Variable
ψ	Matrix osmotic pressure coefficients	ψ_1 = 13.5; ψ_2 = 2,320; $\psi_3 = 1.54 \times 10^5$ (58)	Variable
Ω	Vascular resistance (arterial, capillary, venous, total)	Ω_a = 2.43; Ω_c = 0.12; Ω_v = 0.22; Ω_{tot} = 2.77 (59)	$mmHg \cdot min \cdot ml^{-1}$

Numbers in parenthesis indicate references.